Electromagnetic energy harvesting from vibrations induced by Kármán vortex street

Dung-An Wang*, Chun-Yuan Chiu, Huy-Tuan Pham

Graduate Institute of Precision Engineering, National Chung Hsing University, Taichung 40227, Taiwan, ROC

Abstract

A new electromagnetic energy harvester for harnessing energy from vibration induced by Kármán vortex street is proposed. It converts flow energy into electrical energy by fluid flow, vortex shedding from a bluff body and electromagnetic induction. An analytical design method for the energy harvester is developed. A prototype of the energy harvester is fabricated and tested. The prototype has a volume of 37.9 cm^3. Experimental results show that an output peak-to-peak voltage of nearly 20 mV in average is generated when the excitation pressure oscillates with an amplitude of 0.3 kPa and a frequency of about 62 Hz. By detecting the voltage drop across a matched load, the instantaneous power is determined as 1.77 μW under a pressure fluctuation frequency of 62 Hz and a pressure amplitude of 0.3 kPa in the Kármán vortex street.

Keywords: Electromagnetic; Energy harvester; Kármán vortex street

* Corresponding author. Tel.:+886-4-22840531; fax:+886-4-22858362

E-mail address: daw@dragon.nchu.edu.tw (D.-A. Wang).

1. Introduction

Development of wireless sensor networks for industrial process monitoring and control, machine health monitoring, environment and habitat monitoring, healthcare applications, home automation, and traffic control demands an economical source of energy without supply of fuel and replacement of finite power sources. Applications of wireless sensor networks (WSN) have been limited by battery lifetime and battery size. As reported by Stoianov et al. [1], the battery life for a WSN monitoring a water supplying pipeline was consistent with duration of around 50-62 days. In recent years a considerable effort was focused on the development of energy harvesters or micropower generators for deployment of battery-less or rechargeable battery powered devices [2-7]. By harvesting energy from the environment, miniature sensing/actuating devices can be self-powered in order to avoid the replacement of finite power sources. Sources of energy harvesting can be flowing water [9,10], rain [11], tides [12], wind [13], sunlight [14], and geothermal heat [15].

It may be possible to harvest the fluidic kinetic energy from the motion of fluid. The potential to harvest the energy of fluid motion can be achieved by employing a system that recovers energy from pressure drop, pressure fluctuation, vortex formation in a fluid flow. Krähenbühl et al. [16] designed an electromagnetic harvester based on a turbine driven by water pressure drop in throttling valves and turbo expanders in plants that output a power of 150 W with a rotation speed of 490000 rpm. Their device comprises a turbine and a permanent generator. A detailed electromagnetic machine design, rotor dynamics analysis and a thermal design were required to construct their energy harvester. Holmes et al. [17] reported an axial-flux electromagnetic generator

which was integrated with an axial-flow microturbine to extract power from ambient gas flows. An output voltage of 1.19 V_{pp} was achieved at a rotation rate of 30,000 rpm of their turbine. Herrault et al. [18] presented a rotary electromagnetic generator to harvest the mechanical energy of an air-driven turbine. The devices of Krähenbühl et al. [16], Holmes et al. [17] and Herrault et al. [18] require elaborate techniques for fabrication of their stator-rotor subcomponents and high rotation speeds for efficient energy harvesting.

Erturk et al. [19] presented a piezoelectric composite beam to harvest energy from airflow. Using the self-sustained oscillations of the beam, a maximum output power of 10.7 mW of the piezoaeroelastic system is delivered at an air flow speed of 9.30 m/sec. Akaydm et al. [13] presented a piezoelectric cantilever beam placed in the wake of a circular cylinder to harness energy from air flows. The beam's vibration was caused by the passage of vortices which are formed by vortex shedding from the cylinder. The beam was resonated and placed at the position with maximum generated output power, 4 μW. Sanchez-Sanz et al. [20] accessed the feasibility of using the unsteady forces generated by the Kármán street around a micro-prism in the laminar flow regime for energy harvesting. Allen and Smits [9] used a piezoelectric membrane placed behind the Kármán vortex street formed behind a bluff body to harvest energy from fluid motion. Taylor et al. [21] developed an eel structure of piezoelectric polymer to convert mechanical flow energy to electrical power. They have demonstrated a complete eel system with a generation and storage system in a wave tank. Tang et al. [22] designed a flutter-mill to generate electricity by extracting energy from fluid flow. When flutter takes place, a flexible plate placed between two parallel magnetic panels generates an electric potential. These authors utilized the flow-induced vibrations of fluid-structure

interaction system to extract energy from the surrounding fluid flow [23]. The beam structure of Erturk et al. [19] and Akaydm et al. [13] can provide an output power of several micro-watts, which can be scaled up by increasing the beam size and resonance frequency. The eel structures of Allen and Smits [9], Taylor et al. [21] and Tang et al. [22] have the potential to generate power from milli-watts to many watts depending on system size and flow velocity, but a power-generating eel has not been demonstrated. A device with simpler structure design and ease of application may be needed to extract energy from fluid motion.

One approach to harvest energy is to convert mechanical energy of ambient vibration into electrical energy by electromagnetic induction. Electromagnetic harvesters have been proposed and investigated by many researchers, for example, see [2-7,24-32]. In this paper, we develop a new electromagnetic energy-harvesting device based on vibration induced by Kármán vortex street. As illustrated in Fig. 1(a), a flow channel with a flexible diaphragm is connected to a flow source. A permanent magnet is glued to a bulge on top of the diaphragm and a coil is placed above the magnet. The pressure fluctuation due to vortex shedding from a bluff body drives the diaphragm into vibration. As shown in Fig. 1(b), the increase of the pressure causes the diaphragm to deflect in the upward direction. As the pressure increases to the maximum, the diaphragm reaches its highest position (see Fig. 1(c)). When the pressure drops, the diaphragm moves downward (see Fig. 1(d)). As the pressure decreases to the minimum, the diaphragm reaches its lowest position (see Fig. 1(e)). Thus, by connecting the energy harvester to a flow source, the oscillating movement of the diaphragm with an attached magnet under a coil makes the energy harvesting possible.

The novelty of this energy harvesting approach is the installment of the energy conversion mechanism at the top of the flow channel. This arrangement facilitates the potential of miniaturization of the device using microfabrication, and avoids the need of complex device assembling process. The reported works of energy harvesting from Kármán vortex street [9,21,22] have the eel-like structures placed behind the bluff bodies, their devices require elaborate multi-layered fabrication rendering them unfeasible using microfabrication technologies. Regarding micropower generation devices that utilize axial-flow microturbines [16-18], elaborate techniques for fabrication of their stator-rotor subcomponents and high rotation speeds are required for efficient energy harvesting. Compared to the rotary type harvesters, the presented linear-type device suffers from low power output majorly due to the constraint of energy-conversion efficiency of the piezoelectric materials. This concept of linear-type energy harvesting from Kármán vortex street might pave the way to further miniaturization of feasible devices given the advance of the new nano-structured piezoelectric materials [33].

This paper focuses on the investigation of fluid flow energy extraction by a linear-type harvester using vortex shedding from a bluff body. In order to access the feasibility of the proposed energy harvester, analytical analyses are carried out for design of the device. Fabrication of the energy harvester is described. Experimental setup to measure the pressure, displacement and output voltage of the device is reported. The experimental results are compared with the results of the analyses.

2. Design

2.1 Operational principle

Our design of the electromagnetic energy harvester is based on the vibration induced by vortex shedding from a bluff body. The variation of the liquid pressure in the channel drives a polydimethylsiloxane (PDMS) flexible diaphragm with an attached permanent magnet into vibration. The vibration energy is converted to electrical energy by the Faraday's law of induction [34,35]. An electromagnetic energy harvester is shown in Fig. 2(a). Fig. 2(b) is an exploded view of the energy harvester. It consists of a flow channel with a trapezoidal bluff body placed at the center of the channel, a PDMS diaphragm bonded to the channel, and a permanent magnet glued to an acrylic bulge on top of the PDMS diaphragm. The permanent magnet is placed under a conducting coil which is guided around an inner housing. The inner housing of the coil is fixed by an outer housing. The diaphragm, the magnet and the coil are bounded by a volume of 4 cm (x - Longitudinal) by 4 cm (y- Transverse) by 1.6 cm (z - Thickness). The dimension of the flow channel is 5 cm $\times$ 1.57 cm $\times$ 1.57 cm. The overall volume of the device is 37.9 cm^3.

Flow past a bluff body creates an unstable wake in the form of alternating vortices and induces the periodic pressure variation [36]. The frequency at which the vortices are shed from the bluff body is made non-dimensional using the free-stream velocity U_∞ and a characteristic length ℓ, hence yielding the definition of the Strouhal number, St [37]

$$\mathrm{St} = f\ell / U_\infty \tag{1}$$

where f is the frequency of oscillating flow. The shedding from a circular cylinder immersed in a steady flow occurs in the range $10^2 < \mathrm{Re} < 10^7$, where Re is the Reynolds number, with an average Strouhal number $\mathrm{St} \approx 0.21$ [38].

2.2 Shape of bluff bodies and location of flexible diaphragm

Among the triangular, trapezoidal, circular, ring-type, and conical cylinders, Venugopal et al. [39] found out that trapezoidal bluff bodies are the most appropriate shape in terms of differential pressure amplitude and deviation in Strouhal numbers. For a trapezoidal bluff body, the Strouhal number is given as [40]

$$\mathrm{St} = fH_1 / U_\infty \tag{2}$$

where H_1 is the height of the front side of the trapezoidal cylinder. The front height H_1 and rear height H_2 of the trapezoidal cylinder are denoted in Fig. 2(a).

Williamson [41] stated that a vortex grows in strength until a new vortex forms behind the bluff body, which implies that the point with a maximum velocity fluctuation is half a wavelength downstream of the bluff body. The location with a maximum pressure fluctuation can be assumed as the point with maximum velocity fluctuation for engineering applications. Therefore, the length of the flexible diaphragm can be taken as a wavelength λ, which may be approximated by U_∞ / f. The diaphragm center is positioned at a half wavelength downstream the bluff body in this investigation.

An estimation of the pressure amplitude is needed in order to predict the amplitude of the diaphragm vibration. A nonlinear model of the pressure fluctuation ΔP may be assumed to have the form [42]

$$\Delta P = c \times (\mathrm{Re} - \mathrm{Re}_{crit})^{1/2} \tag{3}$$

where c is a constant and Re_{crit} is a critical Reynolds number. This equation is derived by a linearization of a steady state amplitude solution of a Stuart-Landau nonlinear model equation for the amplitude of wake oscillations [41].

2.3 A quasi-static model for the diaphragm

The displacement of the diaphragm can be estimated by a quasi-static model to describe the kinetics and corresponding output characteristics of the proposed design. A linear elastic model can be used to simulate the elastic deformation of PDMS diaphragm. The liner elastic model is only a first-order approximation for a hyperelastic material like PDMS [43]. Here, the simple model is used as a guideline for design and analysis of the PDMS diaphragm. Fig. 3 is a schematic of the diaphragm under the pressure load P due to the vortex street, the gravitational load W due to the weight of the acrylic and the magnet, and the magnetic force F_{mag} due to the electromechanical coupling. The edges of the diaphragm are assumed clamped. a, b and h represent the length, width and the thickness of the diaphragm, respectively. The gravitational load W is assumed concentrated at the diaphragm center. It is assumed that the pressure load P is uniformly distributed in order to estimate the spring constant of the device. Using Ritz's method [44], the deflection of the diaphragm center w with clamped edges is derived as

$$w = \frac{abP}{4\pi^4 D(\frac{3b}{4a^3}+\frac{3a}{4b^3}+\frac{1}{4ab})} - \frac{W+F_{mag}}{\pi^4 D(\frac{3b}{4a^3}+\frac{3a}{4b^3}+\frac{1}{4ab})} \tag{4}$$

where E and v are the Young's modulus and Poisson's ratio of the diaphragm material, respectively, and D $(=Eh^3/12(1-v^2))$ is the flexural rigidity of the plate. Assuming small F_{mag}, for a differential pressure ΔP and a constant gravitational load W, the differential deflection of the diaphragm Δw can be written as

$$\Delta w = \frac{ab\Delta P}{4\pi^4 D(\frac{3b}{4a^3}+\frac{3a}{4b^3}+\frac{1}{4ab})} \tag{5}$$

and the spring constant of the diaphragm k can be approximated as the ratio of total differential force to the differential deflection

$$k = \frac{\Delta P a b}{\Delta w} = 4\pi^4 D\left(\frac{3b}{4a^3} + \frac{3a}{4b^3} + \frac{1}{4ab}\right) \tag{6}$$

2.4 Electromagnetic induction

The relative movement of the magnet to the coil results in a varying amount of magnetic flux cutting through the coil. According to the Faraday's law of induction, a voltage is induced in the loop of the coil. The voltage induced in the loop of the coil is given as [24]

$$V = \oint_{l_{coul}} (v \times B) \cdot dl \tag{7}$$

where v is the relative velocity of the coil and the magnet, dl is the vector of each segment of the coil, l_{coil} is the total length of the coil, and B is the magnetic flux density at each coil segment. Due to the small displacement of the magnet, it can be assumed that the magnetic flux density B experienced by the coil is nearly constant. Eq. (7) might be expressed as [29]

$$V = -B_{avg} l_{coil} v \tag{8}$$

where B_{avg} is the average magnetic flux density across the relative displacement range of the magnet. The magnetic force on the magnet is given by [24]

$$F_{mag} = B_{avg} l_{coil} i \tag{9}$$

where i is the current in the coil. Due to the symmetry of the geometry and the movement of the magnet, an axisymmetric model of the magnet and the coil is considered. Fig. 4 shows an axisymmetric model of the magnet and the coil. A

cylindrical coordinate system is shown in the figure. The dimensions of the magnet are indicated in the figure. The initial distance of the top surface of the magnet from the bottom of the coil d is 1 mm. The radius R and thickness T of the magnet are 10 mm and 2 mm, respectively. The coil with N (=400) turns is modeled as strands in a rectangle made up of many individual insulated turns. The length L_b and thickness t of the rectangle are 12.5 mm and 1 mm, respectively. A uniform current density is assumed throughout the rectangle. The magnet is made of Nd-Fe-B with a remanent flux density B_r of 1.22 Tesla and a coercive field intensity of 927 kA/m. The magnetic flux density B_{avg} can be written as [45]

$$B_{avg} = \frac{B_r}{2}\left(\frac{d+T}{\sqrt{(d+T)^2 + R^2}} - \frac{d}{\sqrt{d^2 + R^2}} \right) \tag{10}$$

2.5 Lumped model

When the fluctuating pressure is applied on the surface of the diaphragm, the diaphragm oscillates up and down, which causes the magnet to vibrate at a frequency about the same as that of the pressure in the Kármán vortex street. In order to increase the voltage output of the energy harvester under the fluctuating pressure loading, the device should be operated at its resonance frequency. In this investigation, a lumped model is developed to analyze the dynamic behavior of the harvester. Fig. 5 shows a lumped model of the device. A proof mass of m is connected to an inertial frame via a linear spring of stiffness k. Mechanical damping is represented by a dashpot with damping coefficient c. A force due to the pressure load F applied to the proof mass makes it translate in the z direction. The magnetic field B due to the magnet is assumed

constant in time and uniform in proximity to the coil [46]. This movement induces a voltage at the coil terminals and this energy is delivered to a resistive load R_L. i is the current through R_L and the coil. R_e and L_e are the resistance and self inductance of the coil, respectively.

Apply Newton's second law of motion to the mass m

$$m\frac{d^2z}{dt^2} + c\frac{dz}{dt} + kz = -B_{avg}l_{coil}i + F \tag{11}$$

and the voltage induced at the coil terminals U is

$$U = B_{avg}l_{coil}\frac{dz}{dt} - R_e i - L_e\frac{di}{dt} \tag{12}$$

The magnetic losses are neglected in the analysis. The transfer function between the output voltage U and the pressure load F can be expressed as [46]

$$\frac{U}{F} = \frac{R_L B_{avg} l_{coil}}{(Z_e + R_L)(\frac{k}{j\omega} + c + j\omega m) + (B_{avg}l_{coil})^2} \tag{13}$$

where ω is the oscillation frequency of the proof mass m, and $Z_e\,(= R_e + j\omega L_e)$ is the electrical impedance of the coil. The transfer function between the displacement V_z and the pressure load F can be expressed as [46]

$$\frac{V_z}{F} = \frac{R_L + Z_e}{(Z_e + R_L)(\frac{k}{j\omega} + c + j\omega m) + (B_{avg}l_{coil})^2} \tag{14}$$

The average electrical power p_e and mechanical power p_m are given as [46]

$$p_e = \frac{R_L(B_{avg}l_{coil})^2}{2\left|(Z_e + R_L)(\frac{k}{j\omega} + c + j\omega m) + (B_{avg}l_{coil})^2\right|^2} \tag{15}$$

$$p_m = \frac{((R_L + R_e)^2 + (L_e\omega)^2)c + (B_{avg} l_{coil})^2 (R_L + R_e)}{2\left|(Z_e + R_L)(\frac{k}{j\omega} + c + j\omega m) + (B_{avg} l_{coil})^2\right|^2} \tag{16}$$

The conversion coefficient η is defined by p_e / p_m

$$\eta = \frac{(B_{avg} l_{coil})^2 R_L}{((R_L + R_e)^2 + (L_e\omega)^2)c + (B_{avg} l_{coil})^2 (R_L + R_e)} \tag{17}$$

Assuming $|Z_e| \langle\langle R_L$, a second order approximations of the system, Eq. (12), is given as [46]

$$\frac{U}{F} = \frac{(B_{avg} l_{coil} / k)\, j\omega}{1 + (1/k)(c + (B_{avg} l_{coil})^2 / R_L)\, j\omega + (m/k)(j\omega)^2} \tag{18}$$

The damped resonance frequency ω_d can be expressed as

$$\omega_d = \sqrt{1 - \xi^2}\,\omega_n \tag{19}$$

where $\xi = (c + (B_{avg} l_{coil})^2 / R_L) / (2\sqrt{km})$ and $\omega_n\ (= \sqrt{k/m})$ is the natural frequency. Large amplitude vibrations of the device may develop when the vortex shedding is in resonance with one of its resonance frequencies. The resonance desired for energy harvesting is likely to occur for the lower modes of vibration. The second order approximations of the system, Eq. (13), is given as

$$\frac{V_z}{F} = \frac{j\omega / k}{1 + (1/k)(c + (B_{avg} l_{coil})^2 / R_L)\, j\omega + (m/k)(j\omega)^2} \tag{20}$$

Therefore, the displacement amplitude $|Z|$ can be written as

$$|Z| = \frac{1/k}{\left|1 + (1/k)(c + (B_{avg} l_{coil})^2 / R_L)\, j\omega + (m/k)(j\omega)^2\right|} |F| \tag{21}$$

In this investigation, the density of the acrylic and neodymium permanent magnet (NdFeB), composed of neodymium, iron, boron and a few transition metals, are taken as 1400 kg/m^3 and 8100 kg/m^3. Fig. 6 shows the measured engineering stress - engineering strain curve of the PDMS material. The specimens are prepared following the ASTM D 882 test standard for thin plastic sheeting. The tensile tests are performed within 36 hours after the curing of the PDMS material. The Young's modulus of the PDMS material is estimated as 6 MPa based on the engineering stress - engineering strain curve. The Poisson's ratio and density of the PDMS material are taken as 0.5 and 1670 $\mathrm{kg/m^3}$, respectively.

2.6 Analyses

Fig. 7 shows the pressure fluctuation ΔP at the diaphragm center as a function of $(\mathrm{Re}-\mathrm{Re}_{crit})^{1/2}$ based on three-dimensional computational fluid dynamics simulations. The three-dimensional flow analysis is carried out using a commercial software ANSYS CFX. In the analysis, a uniform velocity profile at the inlet along the direction of the inlet flow is applied. No-slip (zero velocity) conditions all along the channel walls are specified. The fluid is considered incompressible. It is assumed that only the relative value of pressure is important, and a zero pressure is applied at the outlet of the channel. The Reynolds number is calculated in order to determine if the analysis is in the turbulent region. The Reynolds number of the flow channel can be determined by

$$\mathrm{Re} = \rho U_\infty H_1 / \mu \tag{22}$$

where U_∞ is the flow velocity at the inlet of the device, μ is the dynamic viscosity of the water, 1.002×10^{-3} Pa$\cdot$sec, and H_1 is the height of the front side of the trapezoidal

cylinder. As shown in Fig. 7, a linear fit of the pressure fluctuation at the diaphragm center is obtained with $c = 11.09$ and $\mathrm{Re}_{crit} = 1813$. An experimental result is also shown in the figure. The result is consistent with the linearization of the Stuart-Landau nonlinear model equation for the amplitude of wake oscillations.

The value of the magnet displacement Δw under the maximum and minimum pressure loading of 3.27 and 2.71 kPa, taken from a typical cycle of pressure history of the experiments, is 56 μm (see Fig. 13(a) and (b)). The simulated Δw based on Eq. (4) corresponding to the pressure cycle is 265 μm, which is much greater than the experimental result. The possible cause for this discrepancy may be the potential issues with PDMS aging. The aging occurs because of changes in internal structure due to curing or other processes [47]. The PDMS material acts soft after casting and then gradually stiffens. Eddington et al. [48] performed accelerated aging experiments of PDMS and showed that the material undergoes a sharp stiffening initially and tapers off with prolonged aging. The Young's modulus is nearly doubled compared to its original value in their experiments. By increasing the value of the Young's modulus of the PDMS material three times, the simulated Δw is 88 μm, which is close to the experimental result. The assembly tolerance and alignment error of the device may also contribute to the discrepancy. With a diaphragm width b of 13 mm instead of 15.17 mm, the simulated Δw is 50 μm, a value much closer to the experimental result. The quasi-static model of the displacement of the magnet can be used for quick evaluation of the effects of the structure dimensions and material properties on the device performance.

The voltage induced in the loop of the coil can be calculated using Eqs. (8) and (10). A velocity history of the magnet needed in Eq. (8) can be obtained by

differentiation of a displacement history of the magnet. Fig. 8(a) shows a typical displacement cycle of the magnet based on the experiments (see Fig. 13 (b)). Fig. 8(b) shows the induced voltage history in the coil. The value of the peak-to-peak voltage is nearly 80 mV_{pp}. Compared to the experimental result of nearly 20 mV_{pp}, the simulation result is much higher. The material properties of the magnet, assembly tolerances and part misalignment may be the reasons for this discrepancy. If the values of the remanent flux density B_r is decreased to 1 Tesla and the initial gap between the top surface of the magnet and the bottom of the coil d is increased to 1.4 mm. the simulated peak-to-peak voltage is 40 mV, which is closer to the experiment.

3. Fabrication, experiments and discussions

3.1 Fabrication

In order to verify the effectiveness of the proposed energy harvesting device, prototypes of the energy harvester are fabricated. The PDMS diaphragm is fabricated by a molding process in an acrylic mold. First, an acrylic mold is carved by a milling machine (PNC-3100, Roland DGA Co., Japan). Next, the PDMS material is poured over the mold. The PDMS material is composed of two parts, a curing agent and the polymer. They are mixed with a volume ratio of 1:10. Before pouring into the mold, the mixture is degassed under vacuum until no bubbles appear. The PDMS is cured at 80^{o}C for 40 minutes. Then, the PDMS is peeled off from the mold.

Fig. 9 shows the assembly steps of the energy harvester. The walls, the top plate and the bottom plate of the flow channel are manufactured by a milling machine. First, the walls are glued to the bottom plate. Next, a trapezoidal bluff body is affixed to the

walls. Then, the top plate of the flow channel with an embedded PDMS diaphragm is attached to the top surface of the walls. Subsequently, an acrylic bulge is glued to the center of the PDMS diaphragm, and a magnet is glued to the top surface of the bulge. Finally, the inner housing with the coil wrapped around its exterior surface is placed inside the outer housing, which is then glued to the top surface of the acrylic blocks to complete the assembly steps. The distance between the top surface of the magnet and the bottom of the coil is 1 mm. Fig. 10 is a photo of an assembled energy harvester. Table 1 lists the dimensions of the prototype and the relevant physical properties.

3.2 Experiments

Fig. 11 is a photo of the experimental apparatus for testing of the fabricated device. The energy harvester is placed on an optical table for vibration isolation. From the bottom of a storage tank, an inlet pipe is run down to the inlet of the energy harvester. The water level in the storage tank is kept constant for a constant pressure drop through the length of the channel. Using gravity, water is forced into the inlet of the energy harvester. Tap water is pumped into the storage tank through a pump located in a recycle tank. An outlet pipe extending between the outlet of the energy harvester and the recycle tank provides a continuous supply of water. Fig. 12 is a schematic of the measurement apparatus. The oscillating displacement of the magnet is measured by a fiberoptic displacement sensor (MTI-2000, MTI Instruments Inc., US). The voltage induced by the coil is recorded and analyzed by a data acquisition unit (PCI-5114, National Instruments Co., US). The pressure in the flow channel is measured with a subminiature pressure sensor (PS-05KC, Kyowa Electronic Instruments Co. Ltd., Japan)

embedded in the bottom plate of the flow channel, nearly 9 mm behind the bluff body and opposite to the flexible diaphragm. The pressure sensor is connected to a data acquisition unit (DBU-120A, Kyowa Electronic Instruments Co. Ltd., Japan).

The experimental results are shown in Fig. 13. Fig. 13(a) shows the pressure history in the flow channel behind the bluff body, where the pressure oscillates with an amplitude of nearly 0.3 kPa and a frequency of 62 Hz. The measured displacement history of the magnet is shown in Fig. 13(b). The measured open circuit voltage induced by the coil is shown in Fig. 13(c). The output peak-to-peak voltage is nearly 20 mV in average. The time history of the experimental results are considered typical of the measurements in a duration of 20 seconds. Figs. 13(d-f) are the power spectral density corresponding to Figs. 13(a-c), respectively, but are based on series of the measurements in the duration of 20 seconds. Fast Fourier transform is used to compute the power spectral density. It can be seen from Figs. 13(d-f) that there is one obvious peak value of 62 Hz. It is evident that the same peak values shown in Figs. 13(d-f) are caused by the pressure fluctuation in the flow channel. The low frequency noise, below 30 Hz, observed in Figs. 13(d-f) can be attributed to the fact that the flows of the experimental setup are always contaminated by ambient noise sources, and the geometry of the bluff body and the walls of the flow channel are not perfectly symmetric and smooth.

The average free-stream velocity U_∞ measured in the experiments is 1.38 m/sec. The calculated Re is nearly 5855, which is turbulent. The frequency of the pressure fluctuation is nearly 62 Hz, see Fig. 13(d), at which the vortices are shed from the bluff body. Using the front height H_1 = 4.25 mm (see Fig. 2), the free-stream velocity U_∞=1.38 m/sec and Equation (2), the corresponding value of St is estimated as 0.19. The

estimated value of St for a trapezoidal bluff body of the experiments might be reasonable compared the value, 0.21, reported by White [38].

In order to evaluate the harvesting system, experiments on the electrical power output of the device are performed. A matched load can be connected to the device to maximize output power. The internal electrical resistance of the device is measured by a LCR meter (WK 4235, Wayne Kerr Electronics, Ltd., UK). The instantaneous power $\tilde{P}$ can be expressed as

$$\tilde{P} = \frac{(\sqrt{2}\tilde{V})^2}{\tilde{R}} \tag{23}$$

where $\tilde{R}$ is the resistance value of the matched load and $\tilde{V}$ is the root-mean-square value of the voltage drop across the matched load. By connecting the matched load of 38 Ω to the device and detecting the voltage drop across the matched load, 5.8 $\mathrm{mV_{rms}}$, the instantaneous power is determined as 1.77 $\mu\mathrm{W}$. For application of power generation, the conversion coefficient η should be close to 1. Using Eq. (17), the conversion coefficient of the device is determined as 0.48 with the damping coefficient $c = 0.01$ and $R_L = 38\,\Omega$ in Eq. (17). Note that with the damping coefficient varied in the range from 0 to 0.05, the conversion coefficient varies from 0.51 to 0.41. Here, a typical value of the damping coefficient is selected for the calculation of a representative conversion coefficient. The energy conversion efficiency of this method, 0.48, is slightly lower than those of an electromagnetic system, 0.51, and a piezoelectric system, 0.52, with similar dimensions [46]. A scaled-up device may provide a higher conversion coefficient and render it more applicable to the purpose of large-scale energy harvesting. With the dimensions of the

coil and magnet scaled up by a factor of one hundred, the conversion coefficient is calculated as 0.85, which is much larger than that of the device.

Most energy harvesting devices based on piezoelectric effects have focused on single-frequency ambient energy, i.e. resonance-based energy harvesting [49]. When the ambient excitation is at a single frequency, the design of the energy harvesting device can be tailored to the ambient frequency available. In this investigation, the device is operated at 62 Hz, which is near its natural frequency ω_n $(=\sqrt{k/m})$ of 60 Hz, determined by the second order approximation of the device. Compared to other researchers' work to extract energy from flow-induced vibrations of fluid-structure interaction system, the presented design might be simpler in its structure and fabrication, since the devices of Holmes et al. [17] and Herrault et al. [18] consist of stator-rotor subcomponents, which need elaborate fabrication steps, and a high rotation speed may be needed for efficient energy harvesting. The eel structure of Allen and Smits [19] has proved to be feasible by simulation and hydrodynamic testing, but a power-generating eel is not demonstrated. Taylor et al. [21] have demonstrated an eel structure with a power generation and storage system in a wave tank. The length, width and thickness of their eel are 9.5", 3", and 0.15 mm, respectively. The challenge to design and deploy a miniaturized eel-like system remains. Although the output power of our device is relatively low, given the structure design of the energy harvester, the dimensions of the device can be decreased for construction of a miniaturized system to harvest energy from vibration induced by Kármán vortex street.

4. Conclusions

An electromagnetic energy harvester based on flow induced vibration is developed. The energy is harvested from Kármán vortex street behind a bluff body in a water flow. The pressure oscillation due to the Kármán vortex street in the flow channel of the harvester results in a periodical displacement of the magnet placed under a coil and therefore the voltage generation. An analytical design method is developed for quick evaluation of the effects of device dimensions, pressure loads and material properties on the performance of the energy harvester. Prototypes of the energy harvester are fabricated and tested. The generated voltage and instantaneous power of the device are approximately 20 mV_{pp} and 1.77 μW, respectively, when the pressure oscillates with an amplitude of nearly 0.3 kPa and a frequency of about 62 Hz. Sources of pressure fluctuation of Kármán vortex street can be geophysical flows (ocean or river currents), air flow in tire cavities, or fluid flow in machinery. The periodic vortex shedding behind a bluff body immersed in a steady stream causes a pressure oscillation in the stream.

Acknowledgement

This work is financially supported by a grant from National Science Council, Taiwan (Grant Number: NSC 99-2221-E-005-075). The authors would like to express their appreciation to the National Center for High-Performance Computing (NCHC), Taiwan for their assistance. Helpful discussions with Professor Jerry M. Chen of National Chung Hsing University, Taiwan, ROC, and Professor An-Shik Yang of National Taipei University of Technology, Taiwan, ROC, are greatly appreciated.

References

[1] I. Stoianov, L. Nachman, S. Madden, T. Tokmouline, Pipenet: A wireless sensor network for pipeline monitoring, in IPSN '07: Proceedings of the sixth International Conference on Information Processing in Sensor Networks. New York, NY, USA: ACM Press, 2007.

[2] C.B. Williams, R.B. Yates, Analysis of a micro-electric generator for microsystems, Sensors and Actuators A 52 (1996) 8-11.

[3] N.N.H. Ching, H.Y. Wong, W.J. Li, P.H.W. Leong, Z. Wen, A laser-micromachined multi-modal resonating power transducer for wireless sensing systems, Sensors and Actuators A 97-98 (2002) 685-690.

[4] P. Glynne-Jones, M.J. Tudor, S.P. Beeby, N.M. White, An electromagnetic, vibration-powered generator for intelligent sensor systems, Sensors and Actuators A 110 (2004) 344-349.

[5] P.-H. Wang, X.-H. Dai, D.-M. Fang, X.-L. Zhao, Design, fabrication and performance of a new vibration-based electromagnetic micro power generator, Microelectronics Journal 38 (2007) 1175-1180.

[6] T. von Büren, G. Tröster, Design and optimization of a linear vibration-driven electromagnetic micro-power generator, Sensors and Actuators A 135 (2007) 765-775.

[7] C.R. Saha, T. O'Donnell, N. Wang, P. McCloskey, Electromagnetic generator for harvesting energy from human motion, Sensors and Actuators A 147 (2008) 248-253.

[9] J.J. Allen, A.J. Smits, Energy harvesting eel, Journal of Fluid and Structures 15 (2001) 629-640.

[10] D.-A. Wang, H.-H. Ko, 2010, Piezoelectric energy harvesting from flow induced vibration, *Journal of Micromechanics and Microengineering*, 20 (2010) 025019.

[11] R. Guigon, J.J. Chaillout, T. Jager, G. Despesse, Harvesting raindrop energy: theory, Smart Materials and Structures, 17 (2008) 015038.

[12] I.G. Bryden and S.J. Couch, Marine energy extraction: tidal resource analysis, Renewable Energy, 31 (2006) 133-139.

[13] H.D. Akaydın, N. Elvin, Y. Andreopoulos, Wake of a cylinder: a paradigm for

energy harvesting with piezoelectric materials, Experiments in Fluids 49 (2010) 291-304.

[14] P.V. Kamat, Meeting the clean energy demand: nanostructure architectures for solar energy conversion, Journal of Physical Chemistry C, 111 (2007) 2834-2860.

[15] R.R. Dickinson, D.L. Battye, V.M. Linton, P.J. Ashman, G.J. Nathan, Alternative carriers for remote renewable energy sources using existing CNG infrastructure, International Journal of Hydrogen energy, 35 (2010) 1321-1329.

[16] D. Krähenbühl, C. Zwyssig, H. Weser, J.W. Kolar, Theoretical and experimental results of a mesoscale electric power generation system from pressurized gas flow, Journal of Micromechanics and Microengineering 19 (2009) 094009.

[17] A.S. Holmes, G. Hong and K.P. Pullen, Axial-flux permanent magnet machines for micropower generation, Journal of Microelectromechanical Systems 14 (2005) 54-62.

[18] F. Herrault, D.P. Arnold, I. Zana, P. Galle, M.G. Allen, High temperature operation of multi-watt, axial-flux, permanent-magnet microgenerators, Sensors and Actuators A 148 (2008) 299-305.

[19] A. Erturk, W.G.R. Vieira, C. De Marqui, Jr., D.J. Inman, On the energy harvesting potential of piezoaeroelastic systems, Applied Physics Letters 96 (2010) 184103.

[20] M. Sanchez-Sanz, B. Fernandez, A. Velazquez, Energy-harvesting microresonator based on the forces generated by the Karman street around a rectangular prism, Journal of Microelectromechanical Systems 18 (2009) 449-457.

[21] G.W. Taylor, J.R. Burns, S.M. Kammann, W.B. Powers, T.R. Welsh, The energy harvesting eel: A small subsurface ocean/river power generator, IEEE Journal of Oceanic Engineering 26 (2001) 539-547.

[22] L. Tang, M.P. Païdoussis, J. Jiang, Cantilevered flexible plates in axial flow: Energy transfer and the concept of flutter-mill, Journal of Sound and Vibration 326 (2009) 263-276.

[23] R.D. Blevins, Flow-induced vibration, 2nd edition, Van Nostrand Reinhold, New York, 1990.

[24] S. Cheng, N. Wang, D.P. Arnold, Modeling of magnetic vibrational energy harvesters using equivalent circuit representations, Journal of Micromechanics and

Microengineering 17 (2007) 2328-2335.

[25] I. Sari, T. Balkan, H. Kulah, An electromagnetic micro power generator for wideband environmental vibrations, Sensors and Actuators A 145-146 (2008) 405-413.

[26] D. Spreemann, D. Hoffmann, B. Folkmer, Y. Manoli, Numerical optimization approach for resonant electromagnetic vibration transducer designed for random vibration, Journal of Micromechanics and Microengineering 18 (2008) 104001.

[27] S. Kulkarni, E. Koukharenko, R. Torah, J. Tudor, S. Beeby, T. O'Donnell, S. Roy, Design, fabrication and test of integrated micro-scale vibration-based electromagnetic generator, Sensors and Actuators A 145-146 (2008) 336-342.

[28] C. Serre, A. Pérez-Rodríguez, N. Fondevilla, E. Martincic, J.R. Morante, J. Montserrat, J. Esteve, Linear and non-linear behavior of mechanical resonators for optimized inertial electromagnetic microgenerators, Microsystem Technologies 15 (2009) 1217-1223.

[29] B. Yang, C. Lee, W. Xiang, J. Xie, J.H. He, R.K. Kotlanka, S.P. Low, H. Feng, Electromagnetic energy harvesting from vibrations of multiple frequencies, Journal of Micromechanics and Microengineering 19 (2009) 035001.

[30] B.P. Mann, N.D. Sims, Energy harvesting from the nonlinear oscillations of magnetic levitation, Journal of Sound and Vibration 319 (2009) 515-530.

[31] N.S. Hudak, G.G. Amatucci, Small-scale energy harvesting through thermoelectric, vibration, and radiofrequency power conversion, Journal of Applied Physics 103 (2008) 101301.

[32] P. Li, Y. Wen, P. Liu, X. Li, C. Jia, A magnetoelectric energy harvester and management circuit for wireless sensor network, Sensors and Actuators A 157 (2010) 100-106.

[33] Y. Xi, J. Song, S. Xu, R. Yang, Z. Gao, C. Hu, Z. L. Wang, Growth of ZnO nanotube arrays and nanotube based piezoelectric nanogenerator, Journal of Materials Chemistry, (19) 2009 9260-9264.

[34] B.S. Lee, S.C. Lin, W.J. Wu, X.Y. Wang, P.Z. Chang, C.K. Lee, Piezoelectric MEMS generators fabricated with an aerosol deposition PZT thin film, Journal of Micromechanics and Microengineering 19 (2009) 065014.

[35] E. M. Purcell, *Electricity and magnetism*, 2nd edition, McGraw-Hill, Boston, US, 2004.

[36] R. Violette, E. de Langre, J. Szydlowski, Computation of vortex-induced vibrations of long structures using a wake oscillator model: Comparison with DNS and experiments, Computers and Structures 85 (2007) 1134-1141.

[37] D.F. Young, B.R. Munson, T.H. Okiishi, A brief introduction to fluid mechanics, John Wiley & Sons Inc., New York, US, 2001.

[38] F.M. White, Fluid Mechanics, McGraw-Hill Co., New York, US, 1986.

[39] A. Venugopal, A. Agrawal, S.V. Prabhu, Influence of blockage of shape of a bluff body on the performance of vortex flowmeter with wall pressure measurement, Measurement 44 (2011) 954-964.

[40] Y.J. Chung, S.-H. Kang, Laminar vortex shedding from a trapezoidal cylinder with different height ratios, Physics of Fluids 12 (2000) 1251-1254.

[41] C.H.K. Williamson, Vortex dynamics in the cylinder wake, Annual Review of Fluid Mechanics, 28 (1996) 477-539.

[42] P.A. Monkewitz, Modeling of self-excited wake oscillations by amplitude equations, Experimental Thermal and Fluid Science 12 (1996) 175-183.

[43] Y.-S. Yu, Y.-P. Zhao, Deformation of PDMS membrane and microcantilever by a water droplet: Comparison between Mooney-Rivlin and linear elastic constitutive models, Journal of Colloid and Interface Science, 332 (2009) 467-476.

[44] S.P. Timoshenko, S. Woinowsky-Krieger, Theory of Plates and Shells, Second Edition, McGRAW-Hill, 1959.

[45] D.K. Cheng, Field and wave electromagnetics, Second Edition, Addison-Wesley, 1989.

[46] G. Poulin, E. Sarraute, F. Costa, Generation of electrical energy for portable devices Comparative study of an electromagnetic and a piezoelectric system, Sensors and Actuators A 116 (2004) 461-471.

[47] A.S. Wineman, K.R. Rajagopal, Mechanical response of polymers, Cambridge University Press, Cambridge, UK, 2000.

[48] D.T. Eddington, W.C. Crone, D.J. Beebe, Development of process protocols to fine tune polydimethylsiloxane material properties, 7th International Conference on

Miniaturized Chemical and Biochemical Analysis Systems, Oct. 5-9, 2003, Squaw Valley, California USA, pp. 1089-1092.

[49] S. Adhikari, M. I. Friswell and D. J. Inman, Piezoelectric energy harvesting from broadband random vibrations, Smart Materials and Structures, 18 (2009) 115005.

List of figures

Table 1. Dimensions of the prototype and relevant physical properties

	Property/dimension	
Flow channel	Effective dimension (mm)	$50 \times 15.7 \times 15.7$
Trapezoidal bluff body	Front height H_1 (mm)	4.25
	Rear height H_2 (mm)	1
PDMS	Dimension (mm)	$30 \times 15.7 \times 1$
	Density ($\mathrm{kg \cdot m^{-3}}$)	1670
	Young's modulus E (MPa)	18
	Poisson's ratio ν	0.5
Magnet	Density ($\mathrm{kg \cdot m^{-3}}$)	8100
	Remanent flux density B_r (Tesla)	1.22
	Radius R (mm)	10
	Thickness T	2
Acrylic	Dimension (mm)	$8 \times 8 \times 10$
	Density ($\mathrm{kg \cdot m^{-3}}$)	1400
Coil	Turns N	400
	Resistance R_e (Ω)	36.78
	Inductance L_e (mH)	5.29
	Total length l_{coil} (m)	34.56

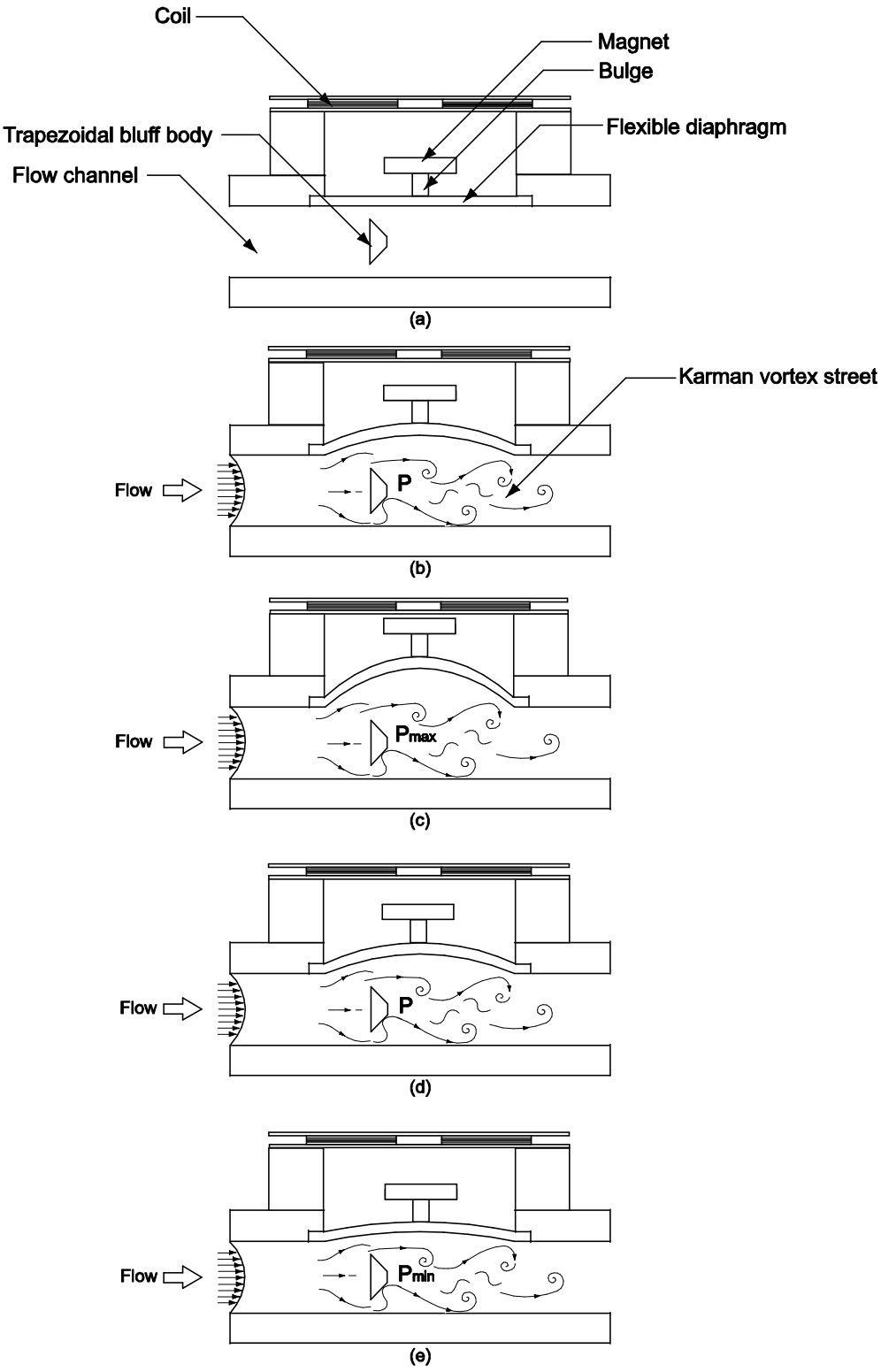

Fig. 1. Operation of an electromagnetic energy harvester.

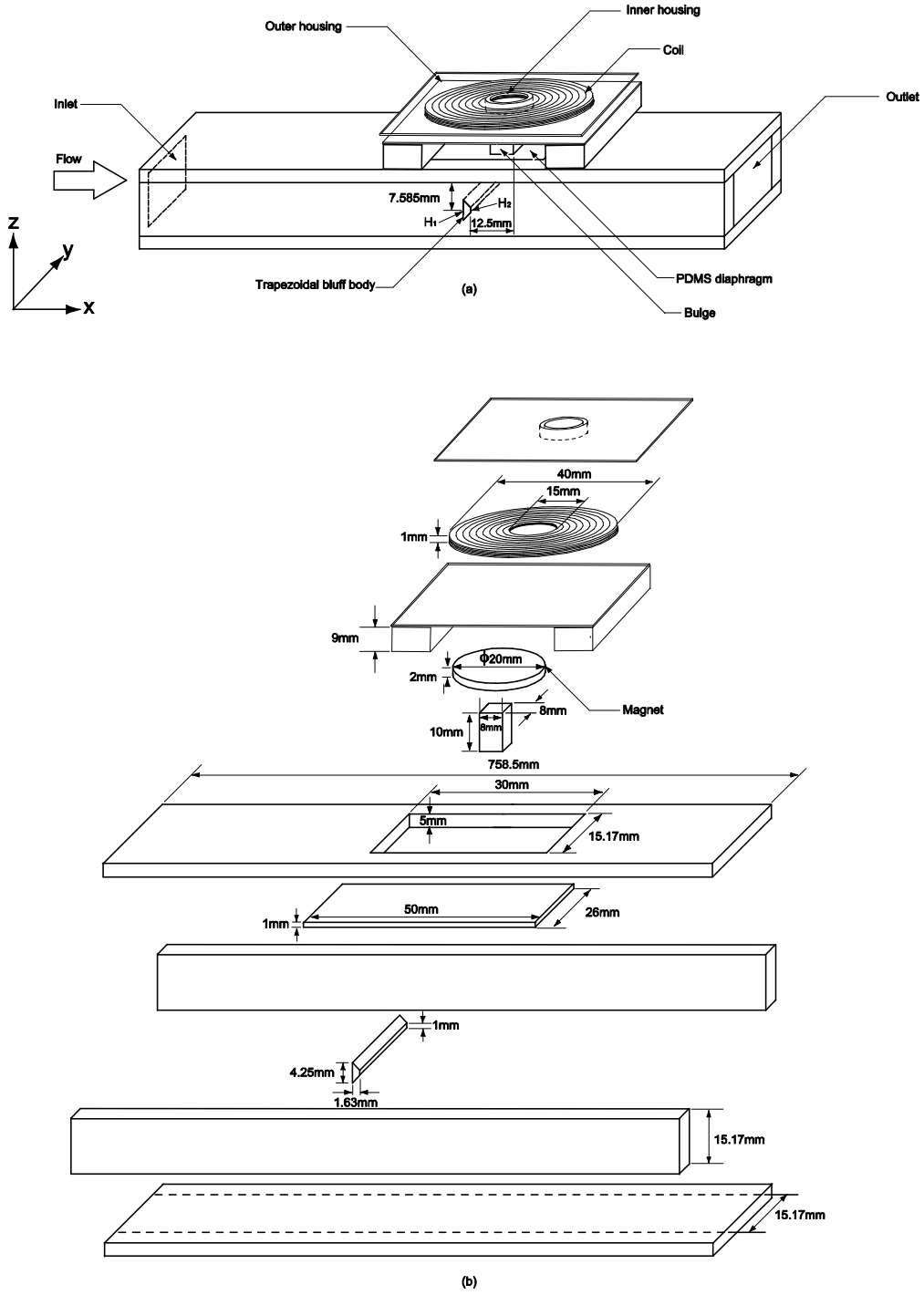

Fig. 2. (a) An assembled energy harvester. (b) Components of the energy harvester.

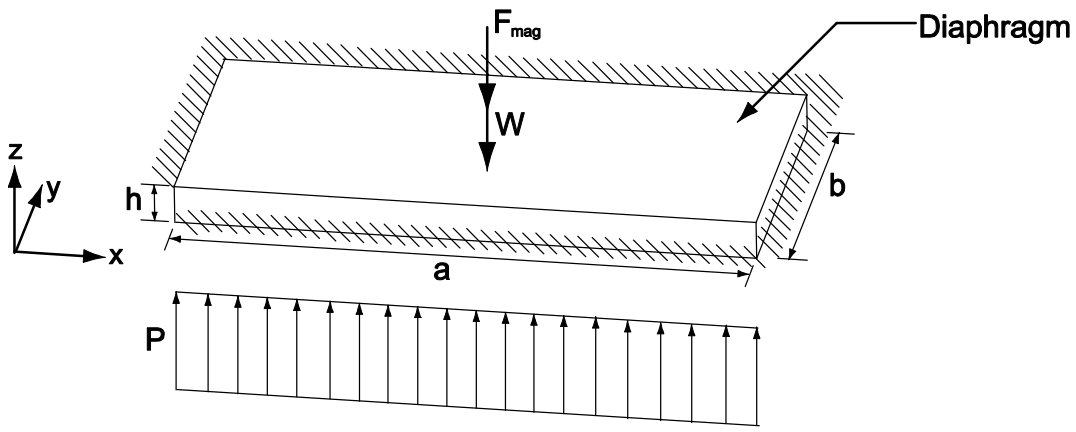

Fig. 3. A schematic of the diaphragm under the loads P, W and F_{mag}.

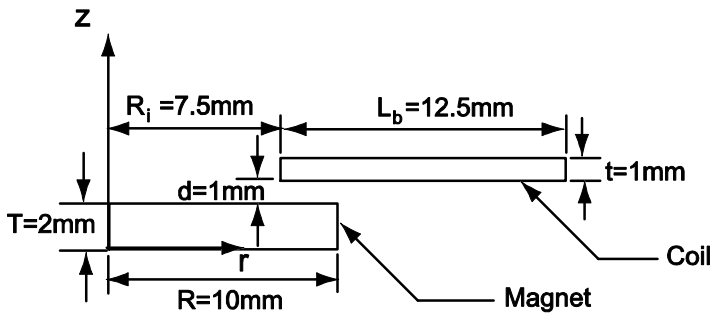

Fig. 4. An axisymmetric model of the magnet and coil.

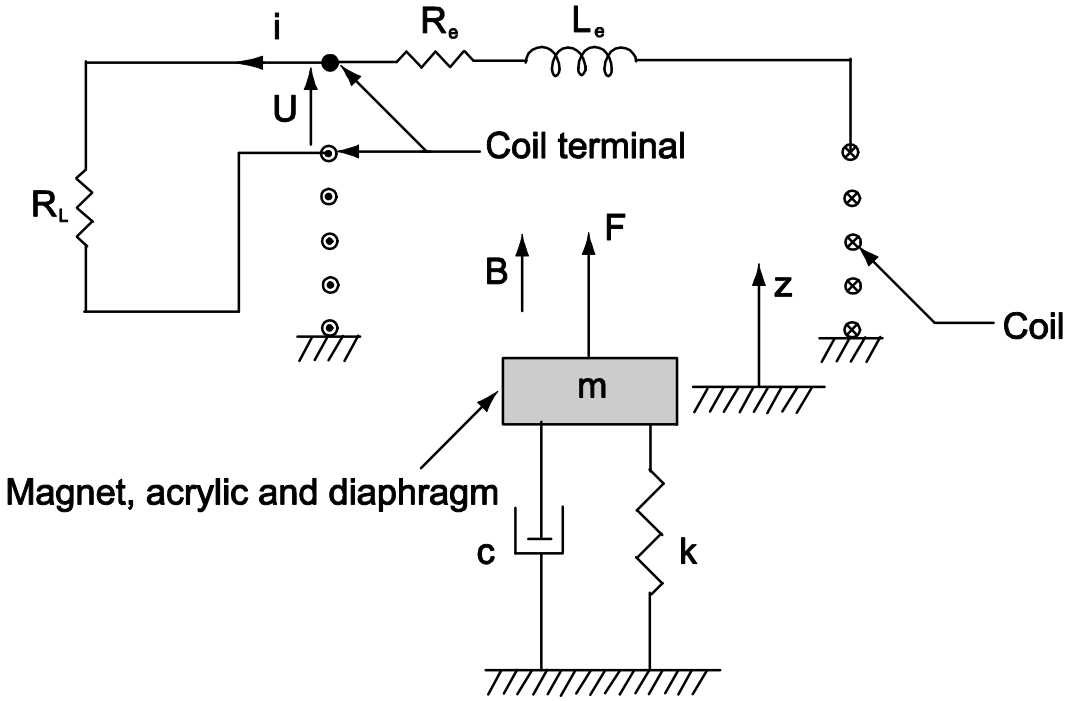

Fig. 5. A lumped model.

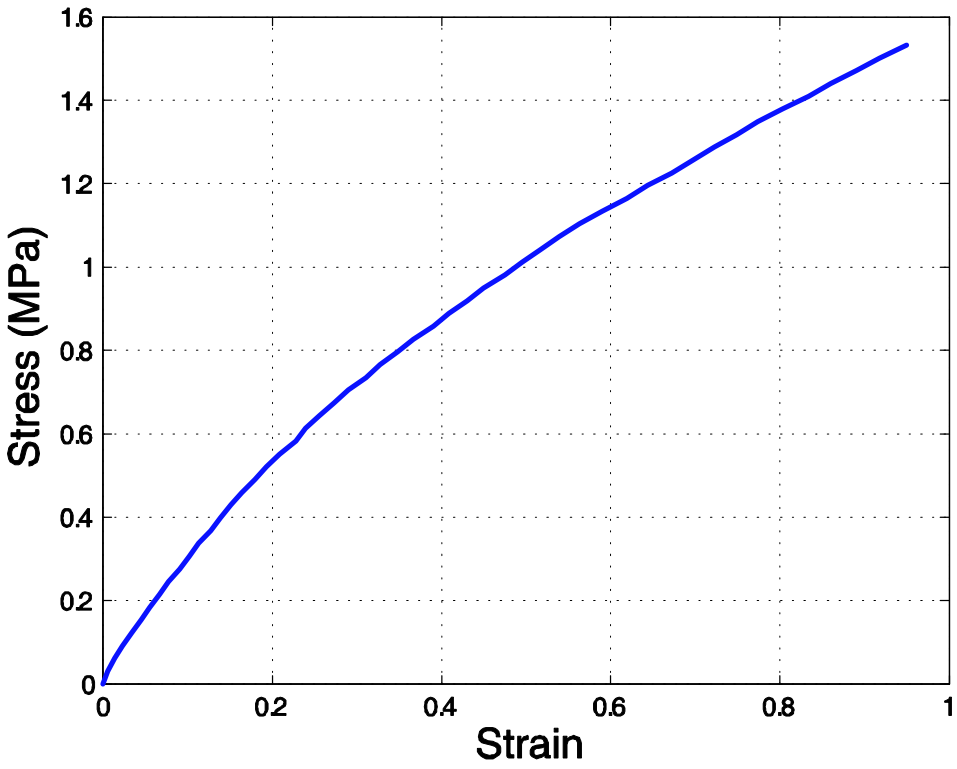

Fig. 6. Measured stress-strain curve of the PDMS material.

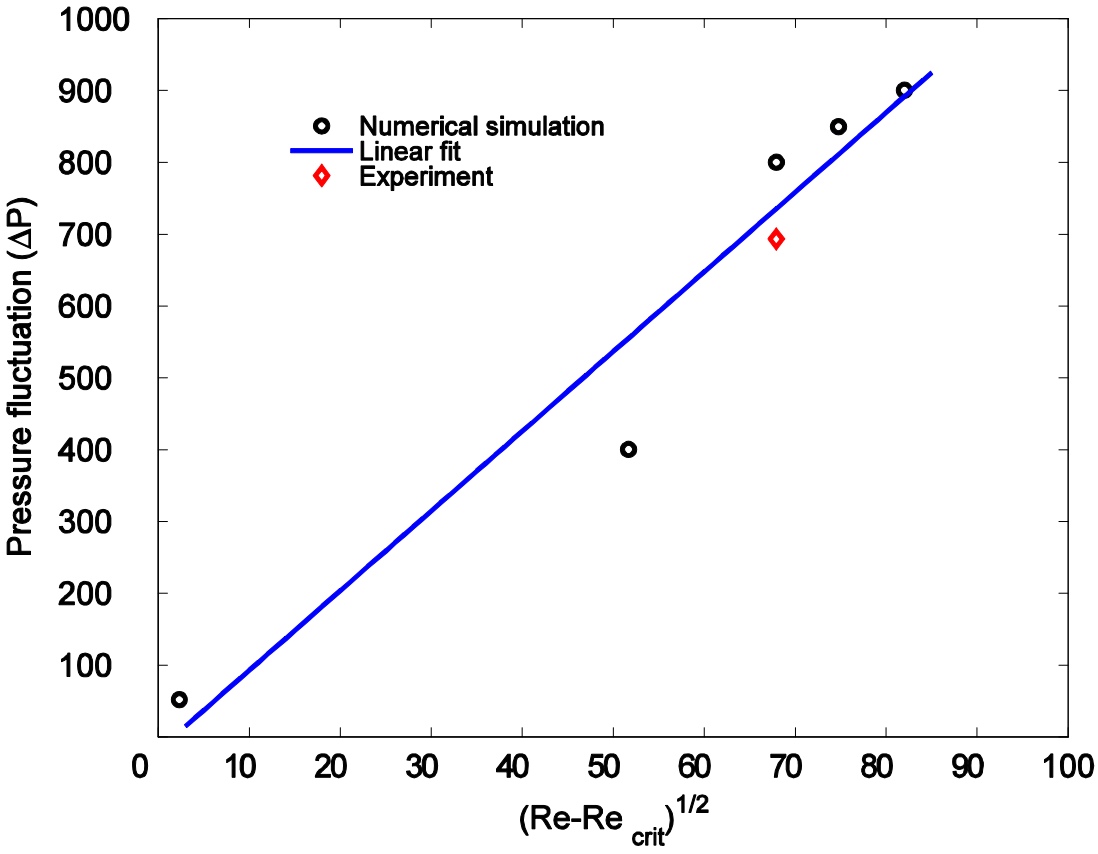

Fig. 7. Pressure fluctuation ΔP as a function of $(\mathrm{Re}-\mathrm{Re}_{crit})^{1/2}$.

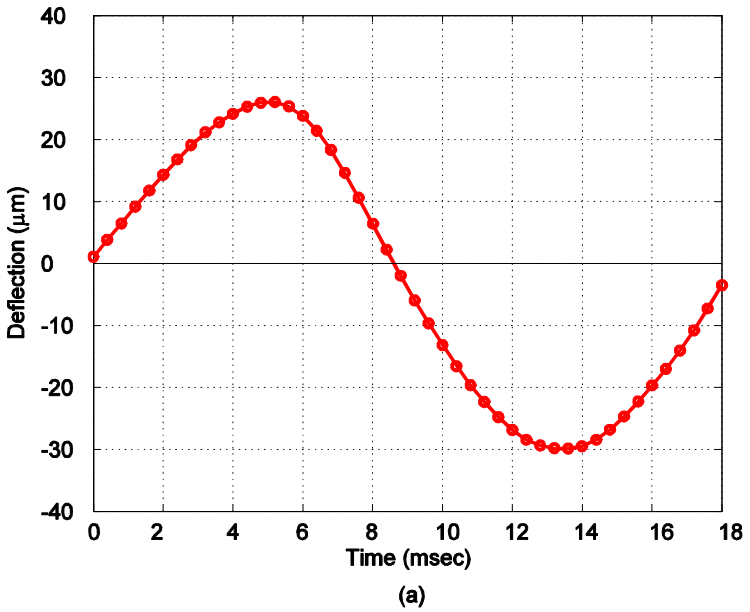

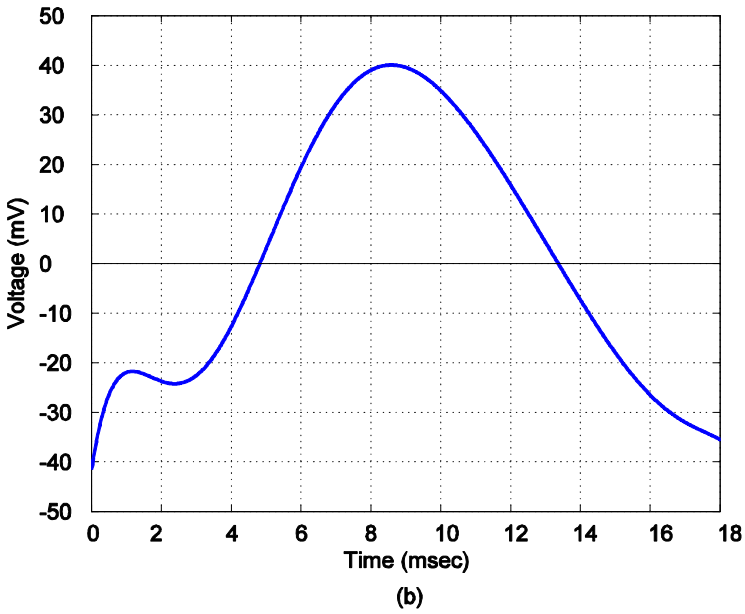

Fig. 8. (a) A typical displacement history of the magnet. (b) Output voltage history.

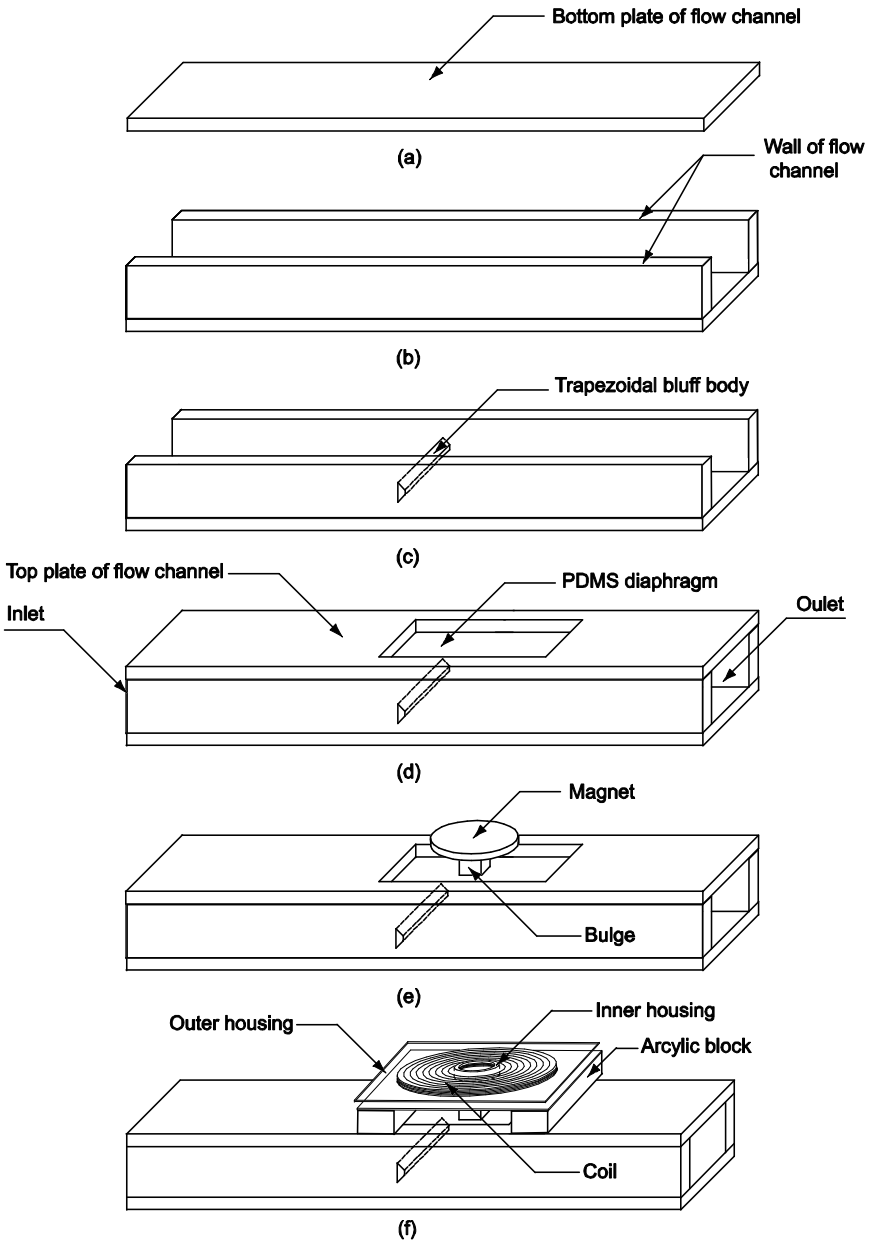

Fig. 9. Assembly steps of the energy harvester.

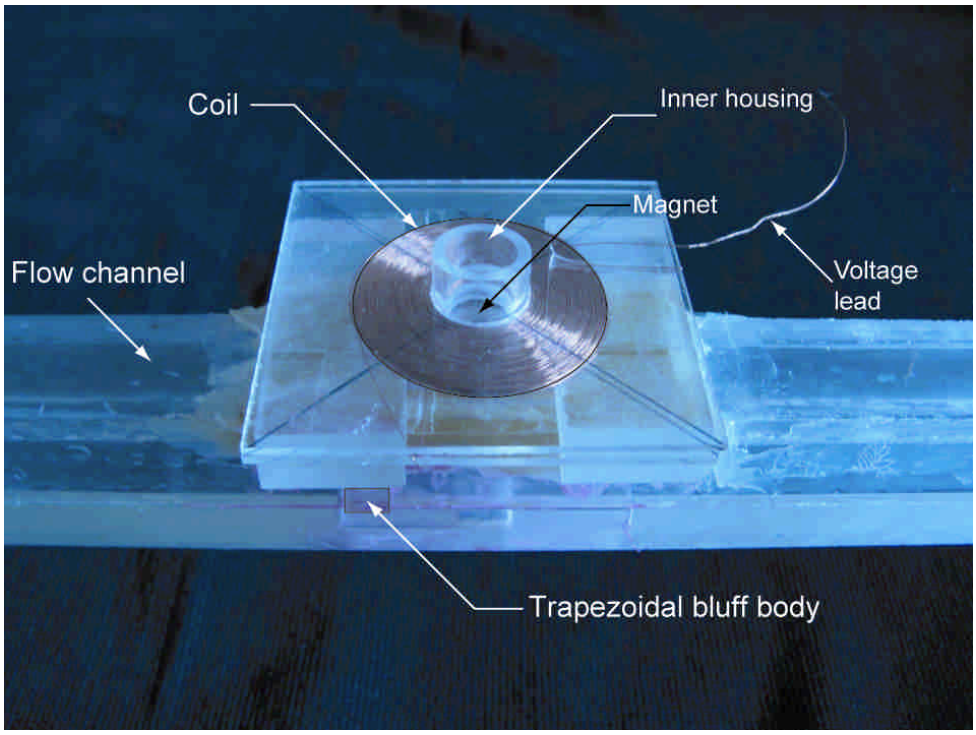

Fig. 10. Assembled energy harvester.

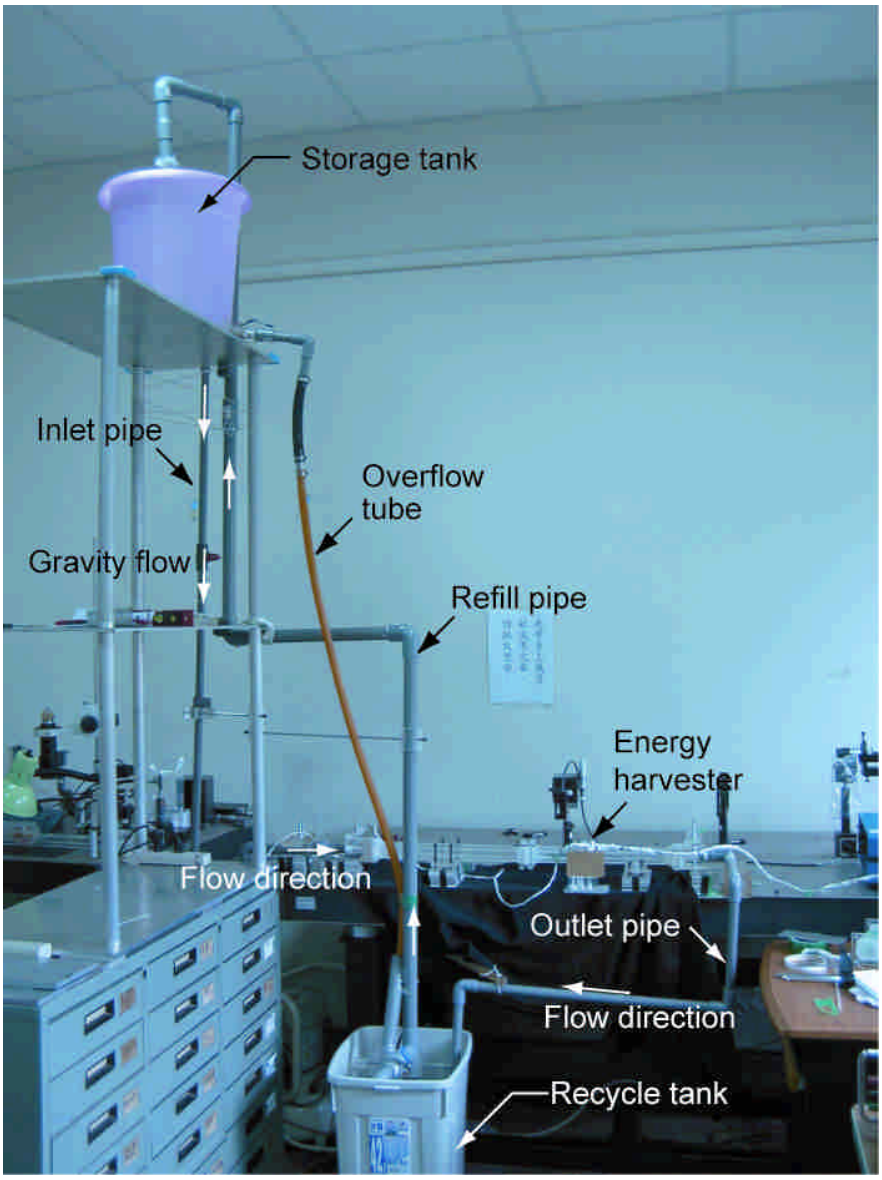

Fig. 11. A photo of the experimental setup.

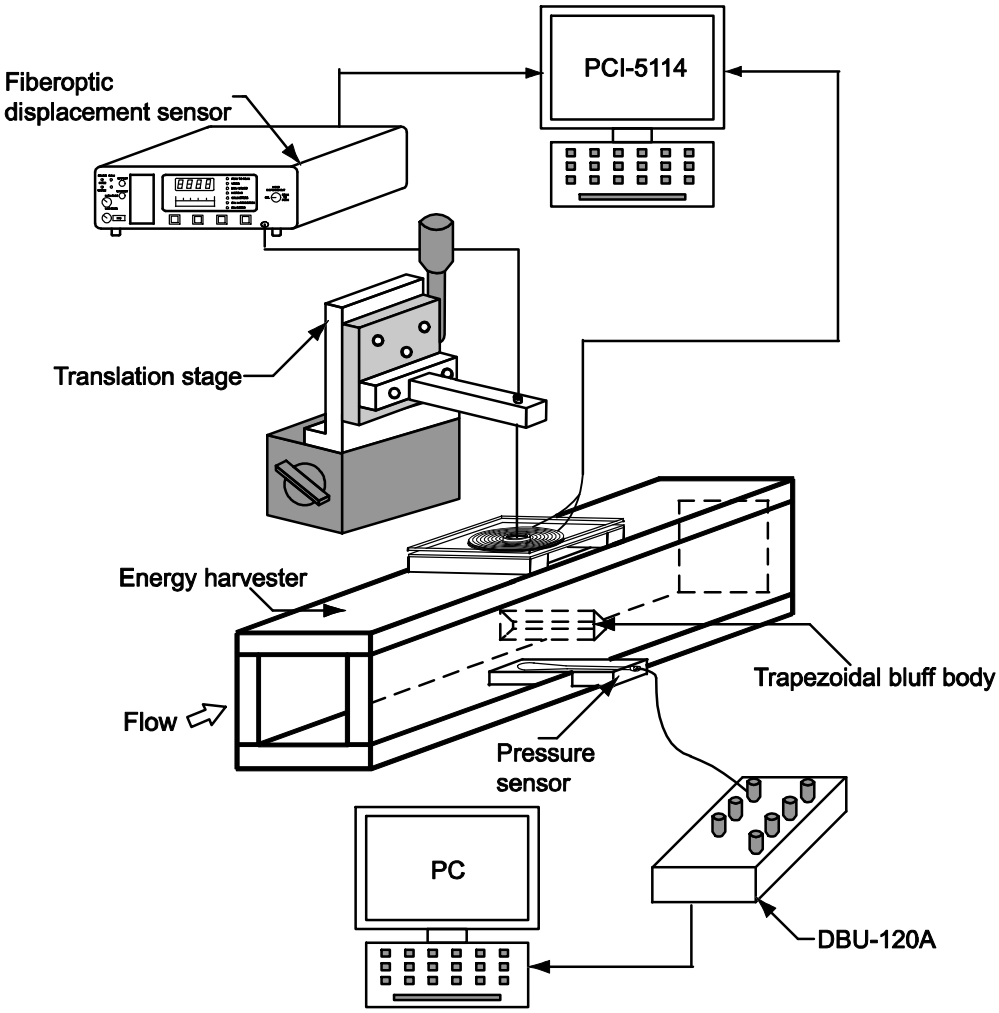

Fig. 12. A schematic of the measurement apparatus.

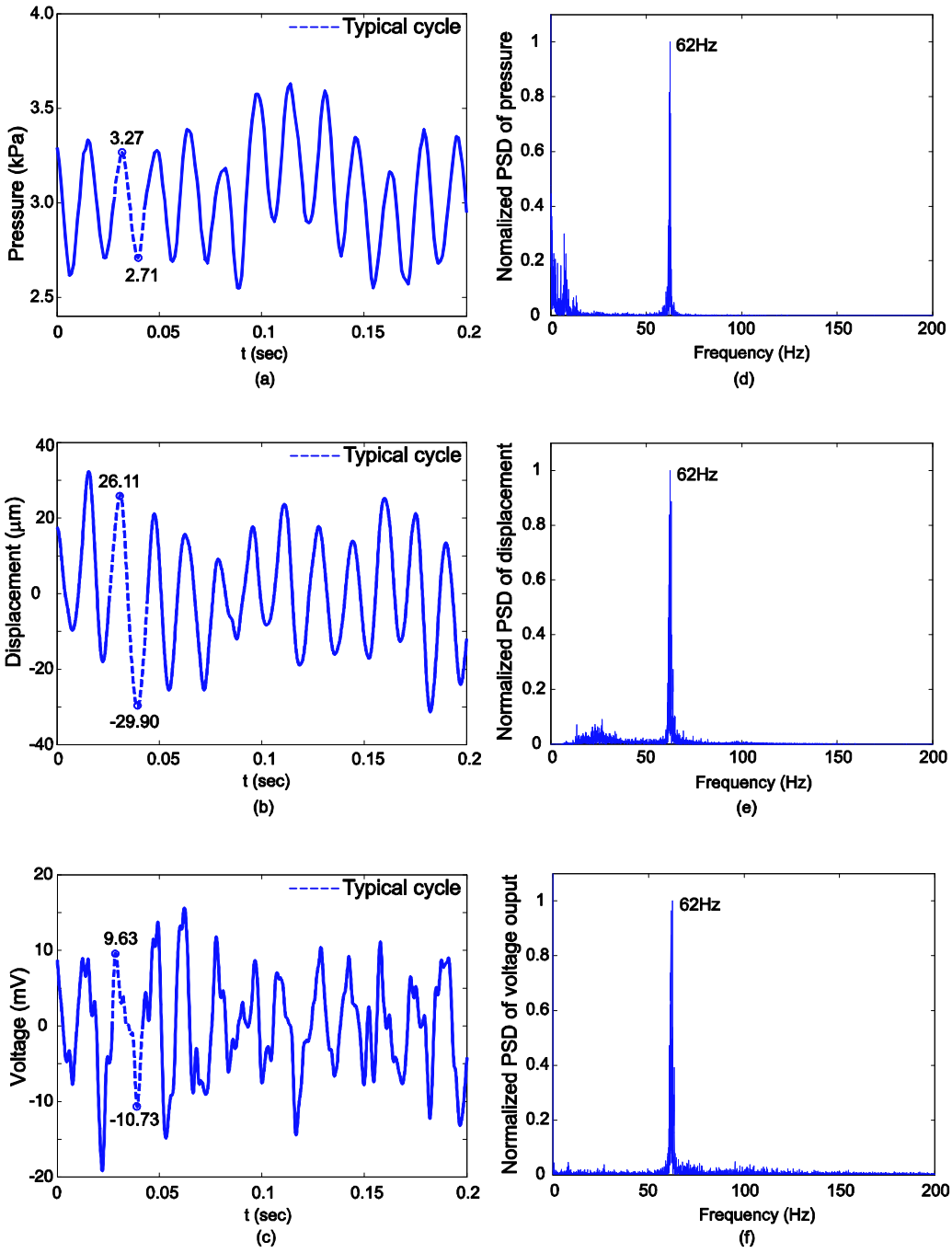

Fig. 13. Experimental results. (a) Pressure variation in the flow channel. (b) Displacement of the magnet. (c) Induced voltage of the coil. (d-f) Power spectral density corresponding to (a-c).